# Molecules at the Quantum−Classical Nanoparticle Interface: Giant Mn$_{70}$ Single-Molecule Magnets of ∼4 nm Diameter

Alina Vinslava,[†] Anastasios J. Tasiopoulos,[†,§] Wolfgang Wernsdorfer,[‡] Khalil A. Abboud,[†] and George Christou*,[†]

[†]Department of Chemistry, University of Florida, Gainesville, Florida 32611, United States
[‡]Institut Néel-CNRS and University Grenoble Alpes, F-38000 Grenoble, Cedex 9, France

Ⓢ *Supporting Information*

ABSTRACT: Two Mn$_{70}$ torus-like molecules have been obtained from the alcoholysis in EtOH and 2-ClC$_2$H$_4$OH of [Mn$_{12}$O$_{12}$(O$_2$CMe)$_{16}$(H$_2$O)$_4$]·4H$_2$O·2MeCO$_2$H (**1**) in the presence of NBu$^n_4$MnO$_4$ and an excess of MeCO$_2$H. The reaction in EtOH afforded [Mn$_{70}$O$_{60}$(O$_2$CMe)$_{70}$(OEt)$_{20}$(EtOH)$_{16}$(H$_2$O)$_{22}$] (**2**), whereas the reaction in ClC$_2$H$_4$OH gave [Mn$_{70}$O$_{60}$(O$_2$CMe)$_{70}$(OC$_2$H$_4$Cl)$_{20}$(ClC$_2$H$_4$OH)$_{18}$(H$_2$O)$_{22}$] (**3**). The complexes are nearly isostructural, each possessing a Mn$_{70}$ torus structure consisting of alternating near-linear [Mn$_3$(μ_3-O)$_4$] and cubic [Mn$_4$(μ_3-O)$_2$(μ_3-OR)$_2$] (R = OEt, **2**; R = OC$_2$H$_4$Cl, **3**) subunits, linked together via *syn,syn-μ*-bridging MeCO$_2^-$ and μ_3-bridging O^{2-} groups. **2** and

3 have an overall diameter of ∼4 nm and crystallize as highly ordered supramolecular nanotubes. Alternating current (ac) magnetic susceptibility measurements, performed on microcrystalline samples in the 1.8−10 K range and a 3.5 G ac field with oscillation frequencies in the 5−1500 Hz range, revealed frequency-dependent out-of-phase signals below ∼2.4 K for both molecules indicative of the slow magnetization relaxation of single-molecule magnets (SMMs). Single-crystal, magnetization vs field studies on both complexes revealed hysteresis loops below 1.5 K, thus confirming **2** and **3** to be new SMMs. The hysteresis loops do not show the steps that are characteristic of quantum tunneling of magnetization (QTM). However, low-temperature studies revealed temperature-independent relaxation rates below ∼0.2 K for both compounds, the signature of ground state QTM. Fitting of relaxation data to the Arrhenius equation gave effective barriers for magnetization reversal (U_{eff}) of 23 and 18 K for **2** and **3**, respectively. Because the Mn$_{70}$ molecule is close to the classical limit, it was also studied using a method based on the Néel−Brown model of thermally activated magnetization reversal in a classical single-domain magnetic nanoparticle. The field and sweep-rate dependence of the coercive field was investigated and yielded the energy barrier, the spin, the Arrhenius preexponential, and the cross-over temperature from the classical to the quantum regime. The validity of this approach emphasizes that large SMMs can be considered as being at or near the quantum−classical nanoparticle interface.
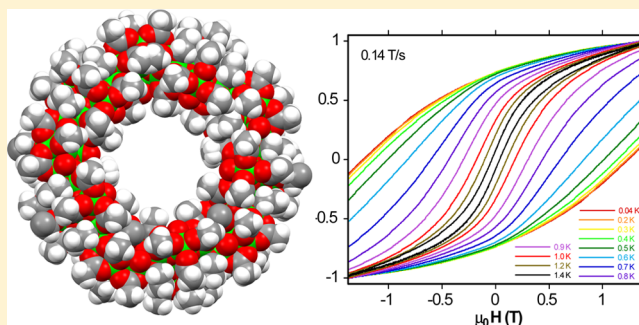
INTRODUCTION

There are several reasons for the continuing interest from groups around the world in single-molecule magnets (SMMs), even though these species function as magnets only at very low temperatures.[1−4] Probably the most important is that they provide a molecular, bottom-up approach to nanoscale magnetism. Each molecule functions as a single-domain magnetic particle that, below its blocking temperature, T_B, exhibits the classical macroscale property of a magnet, namely, magnetization hysteresis. This molecular approach is distinctly different from the traditional top-down approach and brings all the advantages of molecular chemistry to this important area of molecular nanoscience, including mild synthesis conditions, monodispersity, solubility, and a shell of organic ligands that can be postsynthetically modified by standard solution chemistry methods. A particularly crucial advantage has been the crystallinity commonly exhibited by molecular species, providing a means both for attaining structural data at atomic

resolution via single-crystal X-ray crystallography and for permitting detailed studies on highly ordered assemblies in the solid state by a range of spectroscopic and physical methods. The latter has in turn had a profound impact on the quantum physics of nanomagnetism, because single crystals of SMMs are ordered assemblies of monodisperse magnetic particles, usually identically oriented and thus with identical responses to external fields. This has led to the discovery of several novel quantum phenomena within the nanomagnetism field, such as quantum tunneling of the magnetization vector (QTM),[5,6] spin−spin cross relaxation,[7] exchange-biased QTM,[8] quantum superposition states and entanglement,[9] quantum phase interference,[10] and others. As a result, SMMs have been proposed for various applications, such as molecular bits for very high density information storage and as quantum bits for

quantum information processing[11−14] or as components of spintronics devices,[15,16] and others. Such quantum phenomena are extremely difficult, almost impossible, to identify using traditional magnetic nanoparticles, as studies of putative QTM in traditional magnetic particles have shown.[17] Their unequivocal experimental identification was directly dependent on the molecular advantages of SMMs, especially the ability to modify the ligation to optimize a molecular crystal for a particular study with respect to parallel alignment of all molecules, local site symmetry, intermolecular separations, etc.

Although most of the molecular advantages were recognized from the outset, what could not have been predicted was that giant SMMs would one day be obtained that are of comparable and even greater size than the smallest top-down magnetic nanoparticles.[18−20] In other words, that the molecular bottom-up and traditional top-down worlds of nanoscale magnetism would meet. Although the giant Mn_{84} torus SMM was reported over a decade ago, in 2004,[21] it still remains the highest nuclearity SMM and with a diameter of ∼4.3 nm is bigger than many top-down magnetic nanoparticles. Several other giant clusters have been reported since then, such as Fe_{64},[22] Ln_{104} (Ln = Nd, Gd),[23] $La_{60}Ni_{76}$,[24] $Gd_{54}Ni_{54}$,[25] and $Ln_{24}Cu_{36}$ (Ln = Dy^{3+}, Gd^{3+}),[26] but among them only $Dy_{24}Cu_{36}$ possibly displays SMM behavior. Mn_{84} is thus still by far the highest nuclearity SMM, and it retains all the molecular advantages, including crystallinity. Of course, the torus shape means the total number of metal ions is a lot smaller than in a spherical nanoparticle of the same diameter, so that although the bottom-up and top-down approaches overlap in terms of the diameter of the M/O core, they do not do so in terms of the number of interacting metal ions or the resultant magnitude of the Néel vector.[21,27] However, in some ways this can be considered an advantage of giant SMMs in that they have the size and anisotropic shape to make both their visualization on surfaces and organization for use in devices more feasible while still retaining their description as quantum rather than classical magnets.

We therefore sought to expand this area of giant SMMs by exploring whether other giant Mn molecules with a torus (or other) structure might be attainable or whether Mn_{84} is merely a one-off oddity. We herein describe the syntheses, crystal structures, and magnetic characterization of Mn_{70} SMMs with a torus structure that expand the family of giant Mn wheel-like molecules and represent the second largest Mn clusters and SMMs discovered to date. We shall also demonstrate that they straddle the quantum−classical interface by (i) exhibiting the QTM behavior expected of molecular "quantum magnets" and (ii) being of a size that means they can be treated as small classical nanoparticles and therefore be studied using the techniques and models developed for analyzing properties of single-domain "classical magnets".

■ EXPERIMENTAL SECTION

Syntheses. All preparations and manipulations were performed under aerobic conditions at ambient temperature using reagents and solvents as received. $[Mn_{12}O_{12}(O_2CMe)_{16}(H_2O)_4]\cdot4H_2O\cdot2HO_2CMe$ (1)[1c,28] and $N^nBu_4MnO_4$[29] were prepared as described elsewhere.

Caution! Although no such behavior was observed during the present work, organic permanganates are potentially explosive; such compounds should be synthesized and used in small quantities and treated with utmost care at all times. See the detailed warning given elsewhere.[29b]

$[Mn_{70}O_{60}(O_2CMe)_{70}(OEt)_{20}(EtOH)_{16}(H_2O)_{22}]$ (2). To a stirred slurry of 1 (0.425 g, 0.206 mmol) in EtOH (10 mL) was added over a period of 2 min a freshly prepared solution of $N^nBu_4MnO_4$ (0.30 g, 0.83 mmol) in EtOH (8 mL) and glacial acetic acid (0.75 mL, 13

mmol) to give a dark brown solution. This was stirred for a further 5 min and filtered, the filtrate was layered with $MeNO_2$ (20 mL), and the solution was left undisturbed at ambient temperature. X-ray-quality, red-brown crystals of 2·x(solv) slowly grew over several weeks, together with a small amount of a white microcrystalline powder. The crystals were maintained in mother liquor for X-ray crystallography and other single-crystal studies or collected by filtration, washed with $MeNO_2$, manually separated from the white powder by decanting, and dried in vacuum. The yield was 24% based on total Mn. Vacuum-dried material is highly hygroscopic and analyzed as 2·30H₂O·MeNO₂. Anal. Calcd (Found): C, 22.10 (21.84); H, 4.47 (4.13), N, 0.12 (0.10). Selected IR data (KBr, cm⁻¹): 3423 (s, br), 1558(s), 1421(s), 1345(w), 1028(s), 665(w), 618(w), 580(w).

$[Mn_{70}O_{60}(O_2CMe)_{70}(OC_2H_4Cl)_{20}(ClC_2H_4OH)_{18}(H_2O)_{22}]$ (3). The synthetic procedure was the same as that for complex 2 except that 2-chloroethanol was employed as the solvent. After 1 week, red-brown needles of 3·x(solv) were obtained; white microcrystalline powder was only obtained in filtrates monitored for another 2 weeks. The crystals were maintained in mother liquor for X-ray crystallography and other single-crystal studies or collected by filtration, washed with $MeNO_2$, and dried in vacuum. The yield was 0.22 g (37% based on total Mn). Vacuum-dried material analyzed as 3·2MeCO₂H·MeNO₂. Anal. Calcd (Found): C, 21.14 (21.20); H, 3.49 (3.24), N, 0.11 (0.14). Selected IR data (KBr, cm⁻¹): 3419 (s, br), 1576 (w), 1522 (s), 1436 (s), 1056 (w), 1024 (s), 693 (s), 664 (s), 626 (s), 578 (s), 548 (s), 501(w).

X-ray Crystallography. Data were collected at 173 K on a Siemens SMART PLATFORM equipped with a CCD area detector and a graphite monochromator utilizing Mo Kα radiation (λ = 0.71073 Å). Cell parameters were refined using 8192 reflections. A full sphere of data (1850 frames) was collected using the ω-scan method (0.3° framewidth). The first 50 frames were remeasured at the end of data collection to monitor instrument and crystal stability (maximum correction on I was <1%). Absorption corrections by integration were applied based on measured indexed crystal faces. The structures were solved by the Direct Methods in SHELXTL6[30] and refined on F^2 using full-matrix least-squares cycles (Table 1). The non-H atoms were treated anisotropically, whereas the H atoms were placed in calculated, ideal positions and refined as riding on their respective carbon atoms.

For 2·x(solv), the asymmetric unit consists of 1/4 of the Mn_{70} cluster (located on 2/m centers), and an estimate of 5 MeCO₂H and/or MeNO₂, 8 C₂H₅OH, and 8 H₂O molecules of crystallization, so that x(solv) is approximately 20MeCO₂H(MeNO₂)·32C₂H₅OH·32H₂O. All of the solvent molecules were disordered and could not be

Table 1. Crystallographic and Structure Refinement Data for Complexes 2 and 3

parameter	2	3
formula[a]	$C_{212}H_{450}Mn_{70}O_{258}$	$C_{216}H_{424}Mn_{70}O_{260}Cl_{38}$
fw (g mol⁻¹)	10 973.46	12 374.51
space group	C2/m	C2/m
a (Å)	40.264(4)	40.554(4)
b (Å)	52.631(5)	52.190(6)
c (Å)	15.349(2)	17.174(2)
β (deg)	108.878(2)	108.378(1)
V (Å³)	30 776(5)	34 496(6)
Z	2	2
T (K)	173(2)	173(2)
radiation (Å)[b]	0.71073	0.71073
ρ_{calc} (g/cm³)	1.473	1.733
μ (cm⁻¹)	1.474	1.704
R1[c,d]	6.94	6.18
wR2[c,e]	16.23	17.22

[a]Excluding solvent molecules. [b]Graphite monochromator. [c]$I > 2\ \sigma(I)$. [d]$R1 = 100\Sigma||F_o| - |F_c||/\Sigma|F_o|$. [e]$wR2 = 100[\Sigma[w(F_o^2 - F_c^2)^2]/\Sigma[w(F_o^2)^2]]^{1/2}$, $w = 1/[\sigma^2(F_o^2) + [(ap)^2 + bp]$, where $p = [\max(F_o^2, 0) + 2F_c^2]/3$.
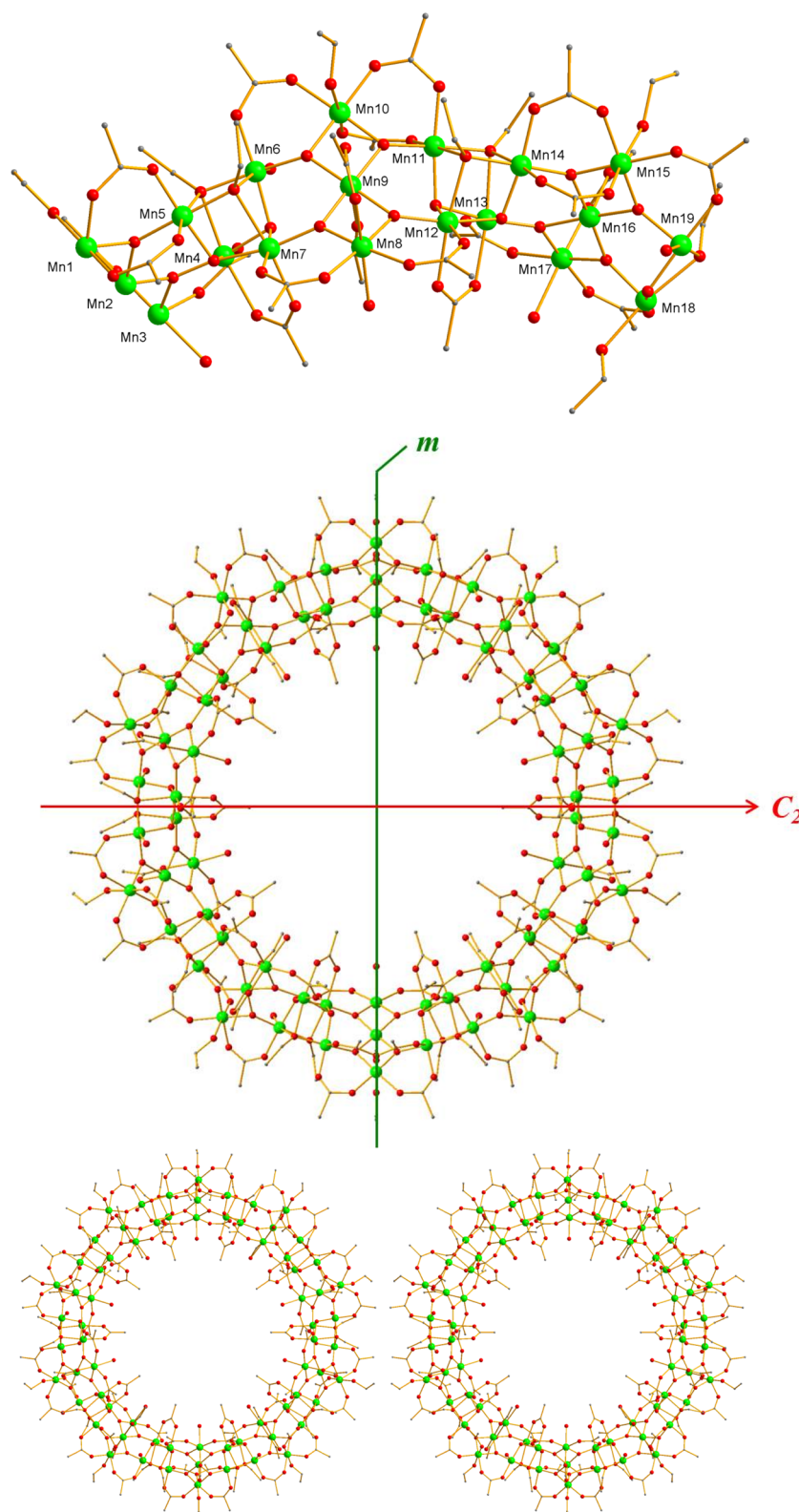
Figure 1. Asymmetric unit (top), the complete structure with crystallographic mirror plane (*m*) and C_2 axis symmetry elements (middle), and a stereopair (bottom) for complex **2**; H atoms are omitted for clarity. Color code: Mn green, O red, C gray.

modeled properly; thus, the program SQUEEZE, a part of the PLATON package[31] of crystallographic software, was used to calculate the solvent disorder area and remove its contribution to the overall intensity data. On the Mn_{70} molecule, one $MeCO_2^-$ ligand bridging Mn1 and Mn5 (and their symmetry partners) is disordered with a H_2O molecule about the mirror plane passing through Mn1 and

bisecting the torus. Mn16 has a disorder between its H_2O and EtOH ligands (50% occupancy each). A total of 1199 parameters were refined in the final cycle of refinement using 64 265 reflections with $I > 2\sigma(I)$ to yield $R1$ and $wR2$ of 6.94 and 16.23%, respectively.

For **3**·*x*(solv), the asymmetric unit consists of 1/4 of the Mn_{70} cluster (again located on $2/m$ centers) and an estimate of 15

$ClC_2H_4OH/MeCO_2H/MeNO_2$ and 10 water molecules of crystallization. The solvent molecules were disordered and could not be modeled properly; thus, the program SQUEEZE was again used to calculate the solvent disorder area and remove its contribution to the overall intensity data. Several ligands on the cluster are disordered: Some $ClC_2H_4O^-$ groups have only their CH_2Cl group disordered, while others also have disorder in their CH_2CH_2 backbone, which refined with 50% occupancy for each part. One $MeCO_2^-$ group, bridging Mn16 and Mn17 (and their symmetry partners), is disordered with a water molecule about the mirror plane through Mn17 bisecting the torus, and the acetate CCH_3 fragments were thus refined with 50% occupancy; the H atoms of the water were not located nor were they included in the final refinement model. A total of 1264 parameters were refined in the final cycle of refinement using 15 761 reflections with $I > 2\sigma(I)$ to yield R1 and wR2 of 6.1 and 17.22%, respectively.

Other Studies. Infrared spectra were recorded in the solid state (KBr pellets) on a Nicolet Nexus 670 FT-IR spectrometer in the 400–4000 cm^{-1} range. Elemental analyses (C, H, and N) were carried out by the in-house facilities of the University of Florida Chemistry Department. Magnetic susceptibility studies were performed at the University of Florida on a Quantum Design MPMS-XL SQUID magnetometer equipped with a 7 T dc magnet and operating in the 1.8–300 K range. Pascal's constants were used to estimate the diamagnetic correction, which was subtracted from the experimental susceptibility to give the molar paramagnetic susceptibility (χ_m). Samples for dc studies were embedded in solid eicosane to prevent torquing. Samples for ac studies in their undried ("wet") form were maintained in mother liquor until needed, removed, patted dry with filter and tissue paper, weighed, and immediately entered into the sample holder for insertion into the SQUID magnetometer. Ultra-low-temperature (<1.8 K) hysteresis loop and dc magnetization relaxation measurements were performed using an array of micro-SQUIDs.[32] The high sensitivity of this magnetometer allows the study of single crystals of SMMs on the order of 10–500 μm. The field can be applied in any direction by separately driving three orthogonal coils.
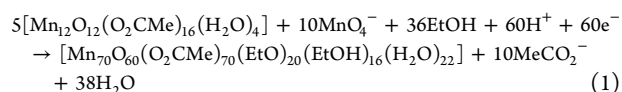
■ RESULTS AND DISCUSSION

Syntheses. A number of new synthetic routes have been developed over the years as a result of efforts to prepare new polynuclear Mn complexes. Some of these include the use of an alcohol as reaction solvent, either by itself or as a mixture. Alcoholysis can occur under such conditions, and the alcohol can thus serve not only as a solvent but also as a source of alkoxide ligands and even as a reducing agent. General categories of such reactions in alcohol include (i) formation of $Mn^{2+/3+}$ clusters from simple salts,[33−35] (ii) alcoholysis of preformed Mn clusters,[21,36] and (iii) our "reductive aggregation" procedure that involves the reduction and aggregation of MnO_4^- in a mixture of alcohol and carboxylic acid.[37,38] These are all undoubtedly very complicated reactions involving multiple aggregation steps, and the exact identity of the product is often sensitive to factors such as the carboxylic acid employed.[38]

The present work involves what could be considered a hybrid of procedures (ii) and (iii), the reaction of the preformed $[Mn_{12}O_{12}(O_2CMe)_{16}(H_2O)_4]$ (**1**) and MnO_4^- in ROH/$MeCO_2H$. We know that if the reaction is carried out in MeOH, the isolated product is the giant $[Mn_{84}O_{72}(O_2CMe)_{78}(OMe)_{24}(MeOH)_{12}(H_2O)_{42}(OH)_6]$ (Mn_{84}) torus mentioned earlier, the highest nuclearity Mn cluster synthesized to date.[21] The formula of Mn^{III}_{84} and its synthesis from $Mn^{III}_8Mn^{IV}_4$ and Mn^{VII} reagents clearly point to MeOH acting as both reducing agent and source of MeO^- ligands, while the acetic acid provides acetate ligands and also maintains the acidic environment to prevent formation of Mn/

O/OH precipitates. An important question now addressed was what would happen if EtOH was used instead of MeOH? How would the small differences in bulk, acidity and other electronic properties between MeOH (pK_a = 15.5) and EtOH (pK_a = 15.9) affect such a complicated reaction, if at all?

The reaction of **1** with $N^nBu_4MnO_4$ in a 1:4 ratio in EtOH/$MeCO_2H$ (8/13 mL) gave a dark brown solution from which was subsequently isolated $[Mn_{70}O_{60}(O_2CMe)_{70}(OEt)_{20}(EtOH)_{16}(H_2O)_{22}]$ (**2**) as highly solvated **2**·*x*(solv). The formation of **2** is complicated, but the main features are summarized in eq 1. A crucial point is that the reaction has an absolute requirement for MnO_4^-; **2** is not obtained if only **1** is dissolved in EtOH/$MeCO_2H$, suggesting that attack of MnO_4^- on **1** is necessary to initiate the reaction, which then obviously includes redox transformations and alcoholysis steps.

$$5[Mn_{12}O_{12}(O_2CMe)_{16}(H_2O)_4] + 10MnO_4^- + 36EtOH + 60H^+ + 60e^-$$
$$\rightarrow [Mn_{70}O_{60}(O_2CMe)_{70}(EtO)_{20}(EtOH)_{16}(H_2O)_{22}] + 10MeCO_2^-$$
$$+ 38H_2O \qquad (1)$$

The overall yield of isolated product is 24%, quite satisfactory for such a complicated reaction. The white byproduct contaminating **2** was a nuisance but could be readily removed manually.

With **2** characterized (vide infra), we also explored the bulkier and less acidic alcohols Pr^nOH, Pr^iOH, Bu^tOH, and others, but these led to bleaching of the reaction colors, i.e., reduction to Mn^{II}, often accompanied by formation of pale yellow or near-white microcrystalline precipitates. We also explored a more acidic alcohol of comparable bulk to EtOH and chose 2-chloroethanol (pK_a = 14.2), which gave persisting brown solutions and subsequent isolation of $[Mn_{70}O_{60}(O_2CMe)_{70}(OC_2H_4Cl)_{20}(ClC_2H_4OH)_{18}(H_2O)_{22}]$ (**3**) as **3**·*x*(solv) in 35–40% yields. In this case, the white byproduct was not a problem, appearing only after crystallization of **3** had been judged complete and the crystals collected by filtration.

Description of the Structures. The structure of **2**, its asymmetric unit comprising 1/4 of the molecule, and a stereopair are shown in Figure 1, and selected bond distances are listed in Tables 2 and S1.[39] The structure can be described as a Mn_{70} torus composed of alternating cubic $[Mn_4(\mu_3-O)_2(\mu_3-OEt)_2]$ and near-linear $[Mn_3(\mu_3-O)_4]$ subunits, 10 of each, linked together via the latter's μ_3-O^{2-} ions and syn,syn-μ-$MeCO_2^-$ groups. The molecule lies on a crystallographic mirror plane passing through two $[Mn_3(\mu_3-O)_4]$ units (Mn1, Mn2, Mn3, and symmetry partners) and a crystallographic C_2 axis bisecting two cubic $[Mn_4O_2(OEt)_2]$ units (Mn18, Mn19, Mn18′, Mn19′, and symmetry partners) (Figure 1a). The molecule thus has crystallographic C_{2h} and virtual D_{5d} symmetry (if the five coordination at two sites is ignored, see below), with the C_5 and collinear S_{10} axes perpendicular to the plane of the torus. The Mn–O bond lengths (Table 2), Mn bond valence sum (BVS) calculations (Table S2),[40,41] and the presence of Jahn–Teller (JT) axial elongations revealed all Mn to be Mn^{III} and near-octahedral, except for Mn2 and its symmetry partner, which are five coordinate with square-pyramidal geometry. O BVS calculations confirmed the degree of protonation of the 60 μ_3-O^{2-}, 20 μ_3-OEt^-, 16 terminal EtOH, and 22 terminal H_2O ligands (Table S3).[42,43] The peripheral ligation consists of 70 syn,syn-μ-$MeCO_2^-$ groups and the terminal EtOH and H_2O molecules, the latter all lying on JT axial positions of the near-linear Mn_3 units. The latter are slightly V-shaped, with Mn–Mn–Mn angles in the range

Table 2. Selected Interatomic Distances (Å)^a for Complex 2

Mn4···Mn5	3.091(3)	Mn6···Mn9	3.447(2)
Mn4···Mn6	3.038(2)	Mn6···Mn10	3.385(2)
Mn4···Mn7	2.838(3)	Mn7···Mn8	3.405(2)
Mn5···Mn6	3.361(2)	Mn7···Mn9	3.411(2)
Mn5···Mn7	3.053(2	Mn8···Mn9	2.808(2)
Mn6···Mn7	3.120(2)	Mn9···Mn10	2.834(2)
Mn4−O48	1.883(6)	Mn7−O15	1.948(9)
Mn4−O52	1.897(6)	Mn7−O14	2.187(7)
Mn4−O50	1.917(7)	Mn7−O53	2.306(8)
Mn4−O8	1.977(8)	Mn8−O56	1.868(7)
Mn4−O9	2.235(8)	Mn8−O54	1.884(7)
Mn4−O51	2.257(7)	Mn8−O17	1.981(8)
Mn5−O50	1.879(7)	Mn8−O19	1.981(7)
Mn5−O49	1.910(7)	Mn8−O16	2.180(9)
Mn5−O11	1.927(9)	Mn8−O18	2.217(7)
Mn5−O53	1.950(7)	Mn9−O54	1.880(6)
Mn5−O10	2.188(9)	Mn9−O56	1.895(6)
Mn5−O51	2.391(8)	Mn9−O57	1.920(7)
Mn6−O55	1.850(6)	Mn9−O55	1.924(7)
Mn6−O52	1.914(6)	Mn9−O20	2.211(8)
Mn6−O51	1.958(7)	Mn9−O21	2.429(15)
Mn6−O13	1.962(7)	Mn10−O57	1.884(6)
Mn6−O12	2.270(7)	Mn10−O55	1.904(6)
Mn6−O53	2.377(8)	Mn10−O25	1.967(7)
Mn7−O54	1.867(6)	Mn10−O24	1.993(7)
Mn7−O52	1.923(7)	Mn10−O23	2.137(8)
Mn7−O50	1.937(7)	Mn10−O22	2.250(8)

^{a}All Mn···Mn separations and Mn−O bonds in one Mn$_7$ repeating unit. See Table S1 for a complete listing of Mn−O bonds in the asymmetric unit.
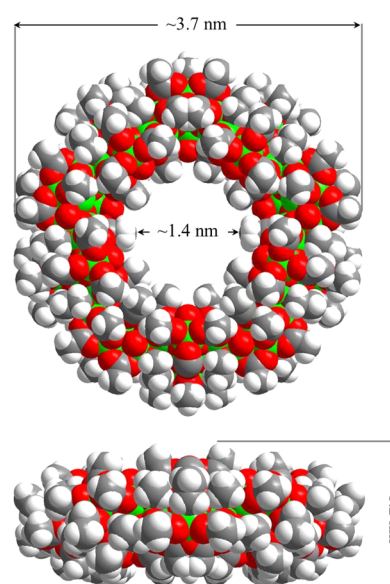

Figure 2. Space-filling representations of **2** (including H atoms) from viewpoints perpendicular (top) and parallel (bottom) to the plane of the torus, showing the dimensions of the molecule and its central cavity.
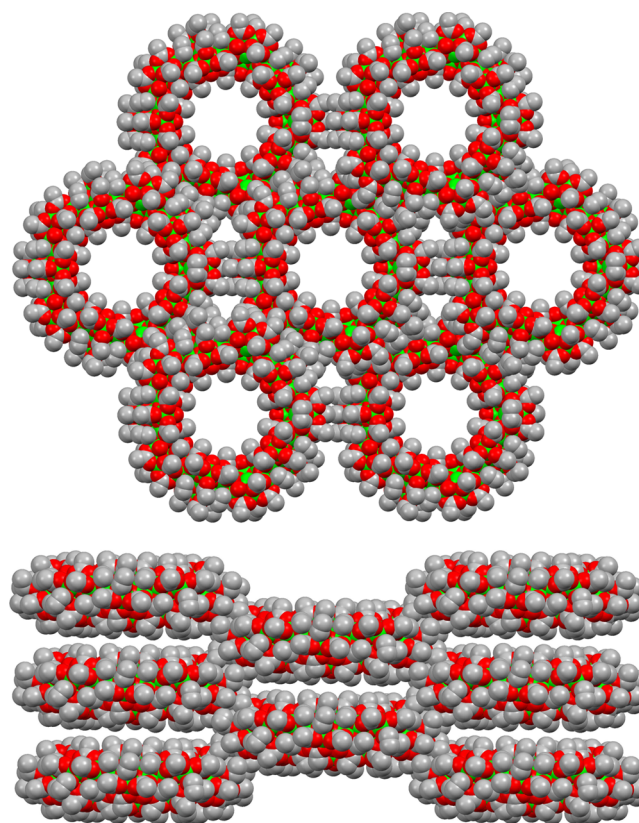

Figure 3. Space-filling representations showing the supramolecular aggregation of **2** into nanotubular columns, viewed (top) along and (bottom) perpendicular to the crystallographic c axis. H atoms are excluded. Color code: Mn green, O red, C gray.

167.3−171.9°. As might be expected, there are many intramolecular O−H···O hydrogen bonds involving EtOH or H$_2$O and acetate or oxide O atoms.

A better representation of the size of **2** is provided by the space-filling plot of Figure 2, which shows that the torus has a diameter of ∼3.7 nm and a thickness of ∼1.2 nm, with a central cavity of ∼1.4 nm diameter and volume ≈ 1.85 nm^3 (1850 Å^3). The molecules order within the crystal to give perfectly cylindrical nanotubular stacks (columns) parallel to the crystallographic c axis (Figure 3) and interdigitating with neighboring columns; thus, molecules in neighboring columns are offset in an *ABAB* manner (Figure 3a). The packing is similar but distinctly different than that previously seen for the Mn$_{84}$ torus, which also forms nanotubular columns but that are not interdigitated.[21]

Crystals of **3**·x(solv) are isomorphous with those of **2**·x(solv), and a superposition of the Mn/O cores of **2** and **3** is shown in Figure S6. The only significant difference between the two molecules, other than the different alcohol employed and small changes to unit cell parameters, is two additional ClC$_2$H$_4$OH ligands in **3**, making the two five-coordinate Mn^{III} in **2** now become six coordinate. The structure is shown in Figure 4, and the asymmetric unit, packing diagrams, selected bond distances, and BVS tables are available in the Supporting Information.[39] The molecule again has crystallographic C_{2h} and virtual D_{5d} symmetry (now all Mn are six coordinate). The Mn are again all Mn^{III},[44] and O protonation levels are as formulated.[45] The molecule has a bigger diameter than **2** of ∼4.1 nm due to the Cl atoms, but the thickness and the diameter of the central cavity are still ∼1.2 and ∼1.4 nm,

respectively. The crystal packing is the same as **2** (Figure S1). Again, there are many intramolecular O−H···O hydrogen bonds throughout the torus and also some OH···Cl ones (O··· Cl = 3.135 Å) involving H$_2$O on one molecule and ClC$_2$H$_4$O$^−$
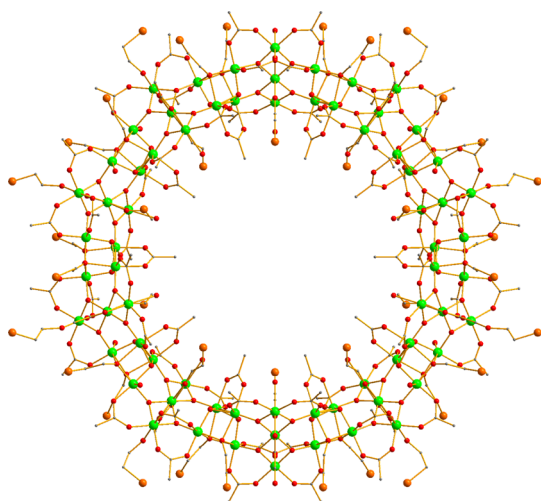
Figure 4. Structure of **3**, with H atoms omitted. Color code: Mn green, O red, Cl orange, C gray.

ligands on a neighbor. Finally, we note that the Mn_{70} nuclearity is the second highest in Mn chemistry after Mn_{84} to be discovered, the next highest being Mn_{44},[46] Mn_{32},[47−49] and Mn_{30}.[50]

Comparison with the Mn_{84} Torus. Apart from their different size, the Mn_{70} and Mn_{84} complexes are similar, both possessing a torus structure comprising the same alternation of cubic $[Mn_4O_2(OR)_2]$ and near-linear $[Mn_3O_4]$ subunits, 10 and 12 of each, respectively. The means of attachment of the subunits is the same, as is the relative disposition of the peripheral ligands. For example, in **2** and **3** it is 10 and 12 acetate groups, respectively, that occupy the positions on the inner surface of the torus in the plane of the molecule. In addition, both Mn_{70} and Mn_{84} pack as linear nanotubular columns forming parallel channels in the crystal, the only difference being the interdigitation of the columns for Mn_{70}. As a result of the latter, Mn_{70} molecules in adjacent columns are not in registry, whereas the Mn_{84} ones are, forming 2-D planes of molecules perpendicular to the column direction; the intracolumn separation of Mn_{70} (closest C···C distance = 4.3 Å) is greater than Mn_{84} (3.8 Å) for the same reason.

Mn_{70} and Mn_{84} are thus members of a family of cyclic structures comprising different numbers of Mn_7 units, and it suggests that others might be attainable. In fact, because of a twist of the constituent Mn_4 and Mn_3 subunits back and forth around the ring, it is better to describe Mn_{70} and Mn_{84} as containing five and six Mn_{14} repeating units, respectively, as reflected in the D_{5d} and D_{6d} virtual symmetries, i.e., two cubic Mn_4 and two linear Mn_3 subunits. Thus, the closest other members of this family would be Mn_{56} and Mn_{98} tori comprising 4 and 7 repeating units, respectively.

An important follow-up question is why does the alcoholysis polymerization reaction lead to large Mn_{70} and Mn_{84} torus structures rather than 1-, 2-, or 3-D polymers? The possible answer is suggested by $[Mn_{11}O_{10}Cl_2(O_2CMe)_{11}(bpy)_2$-$(MeCN)_2(H_2O)_2]$,[51] a Mn_{11} cluster reported many years ago that contains two $[Mn_4O_3Cl]$ cubanes either side of a near-linear $[Mn_3O_4]$ unit (Figure 5), i.e., it is very similar to a fragment of the torus structure except that the cube contains three μ_3-O^{2-} and one μ_3-Cl^- rather than two μ_3-O^{2-} and two μ_3-OR^-. This Mn_{11} core clearly has an intrinsic curvature, and we speculate that such a curved unit forming during the
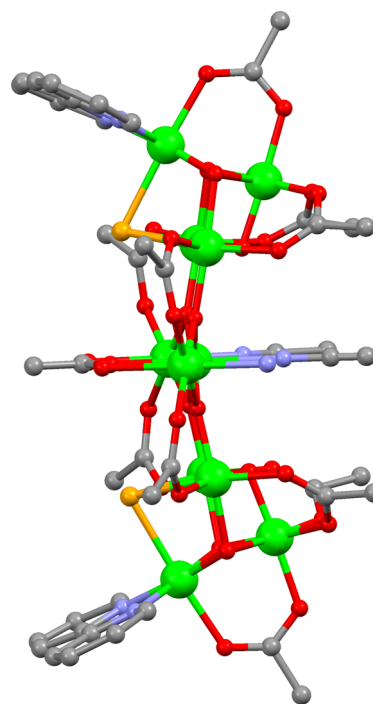
Figure 5. Mn_{11} cluster mentioned in the text that is a fragment of the Mn_{70} structure emphasizing the intrinsic curvature that is proposed to explain the molecular torus rather than polymeric structure of **2** and **3**.

alcoholysis polymerization that then grows longer at each end will eventually form a closed loop rather than a polymeric chain. This also suggests an answer to a further question, why EtOH and MeOH yield different nuclearity products. The size of the obtained loop will depend on the degree of curvature, and since a large number of the RO^-/ROH are in groups of three on the outer surface of the torus, our hypothesis is that the greater bulk of Et vs Me will cause an increase in the curvature of the growing polymer and thus formation of a smaller torus. In Figure S2 is shown the Mn_{70} with the Et groups on the outer surface in yellow to emphasize their proximity; attempts to open the torus by an amount required to insert another Mn_{14} unit would be resisted by the resulting steric hindrance. The formation of Mn_{70} torus **3** using 2-ClC_2H_4OH supports that it is not the electronic properties of the alcohol that are important, and the Cl at the 2 position does not introduce additional steric hindrance. Our unsuccessful attempts mentioned earlier to use alcohols with Me substituents at the 1 position (e.g., ^iPrOH) were targeted at increasing the curvature further and possibly obtaining the Mn_{56} torus. Attempts are continuing.

Magnetochemistry. Direct Current Magnetic Susceptibility Studies. Solid-state, variable-temperature magnetic susceptibility (χ_M) measurements were performed on vacuum-dried microcrystalline samples of $2\cdot30H_2O\cdot MeNO_2$ and $3\cdot 2MeCO_2H\cdot MeNO_2$, suspended in eicosane to prevent torquing, in the 5.0−300 K range in a 1 kG (0.1 T) magnetic field. The data, plotted as $\chi_M T$ vs T in Figure 6, show the two complexes to be magnetically similar, as expected from the similar structures. For **2**, $\chi_M T$ decreases gradually from 149.35 cm^3 K mol^{-1} at 300 K to 84.14 cm^3 K mol^{-1} at 50 K and then decreases more rapidly to 26.45 cm^3 K mol^{-1} at 5.0 K. For **3**, the $\chi_M T$ value decreases steadily from 167.58 cm^3 mol^{-1} K at 300 K to 100.84 cm^3 mol^{-1} K at 50 K and then to 28.23 cm^3 K mol^{-1} at 5.0 K. For both complexes, $\chi_M T$ at 300 K is
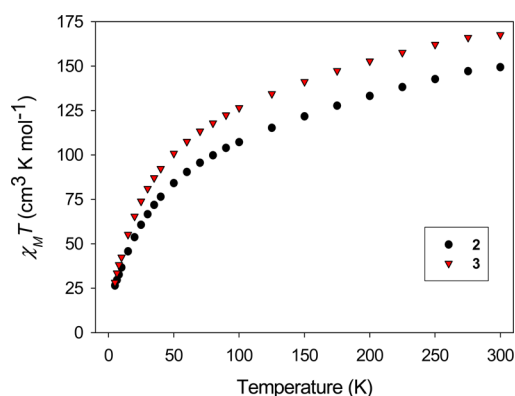
Figure 6. Plots of $\chi_M T$ vs T for dried **2** and **3** in a 0.1T dc field.

significantly lower than the spin-only ($g = 2$) value of 210 cm^3 K mol^{-1} expected for 70 noninteracting Mn^{3+} ions, indicating dominant antiferromagnetic (AF) exchange interactions within the complexes. $\chi_M T$ for **2** is noticeably smaller than for **3**, suggesting the exchange couplings are stronger on average in **2** vs **3**.

For such a high-nuclearity system of exchange-coupled Mn^{3+} ions there will be a very high density of spin states, likely approaching a classical-like continuum. As expected, attempts to fit magnetization (M) vs field (H) and temperature data for **2** and **3** collected in the 0.1−7.0 T field and 1.80−10 K temperature ranges using the program MAGNET[52] were unsuccessful. This program assumes only the ground state is populated at these temperatures, includes axial ZFS and the Zeeman interaction with the applied field, and carries out a full powder average. The high density of low-lying excited states invalidates the main assumption of this approach, even when data collected at the higher fields and higher T were excluded. Plots of $M/N\mu_B$ vs H/T, where N is Avogadro's number and μ_B is the Bohr magneton (Figure S3),[39] show the steadily increasing magnetization with field characteristic of field-induced crossings of low-lying excited states with the ground state. Interestingly, $M/N\mu_B$ for **2** is markedly smaller than for **3** at each field, consistent with stronger exchange couplings in the former and supporting the conclusion from the $\chi_M T$ vs T plots. Problems from low-lying excited states are common with higher nuclearity Mn clusters and have been discussed in more detail elsewhere.[37,38,50] A better means to probe the lowest spin states of **2** and **3** and also their magnetization relaxation dynamics is by ac susceptibility studies, which preclude complications from an applied dc field.

Alternating Current Magnetic Susceptibility Studies. Alternating current (ac) susceptibility studies were performed on both vacuum-dried and "wet" (as-isolated from mother liquor) microcrystalline samples of **2** and **3** in the temperature range 1.8−10 K in a zero dc field and a 3.5 G ac field at oscillation frequencies (ν) ranging from 5 to 1500 Hz. The in-phase ($\chi'_M T$) and out-of-phase (χ''_M) signals for wet samples of **2**·x(solv) and **3**·x(solv) are shown in Figures 7 and 8, respectively; the vacuum-dried samples gave essentially identical profiles (Figures S4 and S5). For **2**·x(solv), $\chi'_M T$ decreases steeply below 10 K from 39.01 cm^3 K mol^{-1} to a near-plateau value of ~27 cm^3 K mol^{-1} at ~2.5 K, indicating a high density of low-lying excited states with spin S greater than the ground state, as expected from the high nuclearity. Below ~2.5 K, there is a frequency-dependent decrease in $\chi'_M T$ concomitant with the appearance of frequency-dependent χ''_M

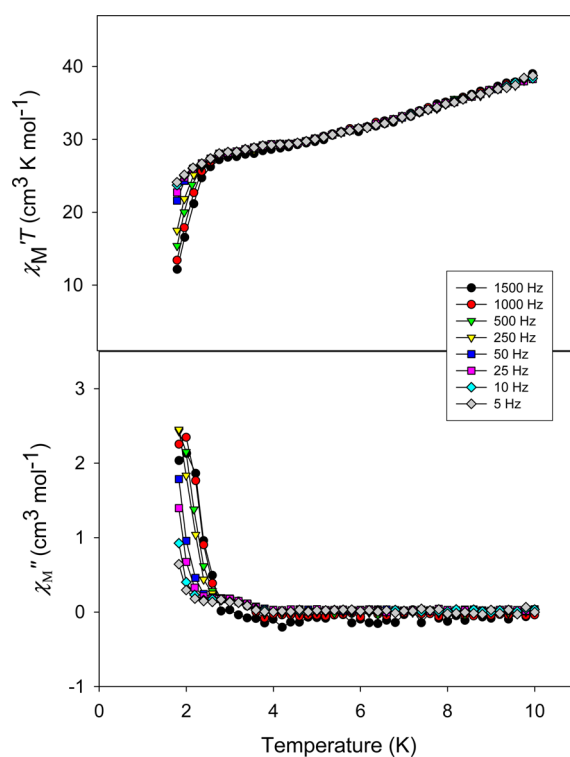**Figure 7.** Plots of the in-phase (χ'_M, as $\chi'_M T$) and out-of-phase (χ''_M) ac magnetic susceptibility vs T for an undried microcrystalline sample of **2**·x(solv) at the indicated oscillation frequencies.

Figure 8. Plots of the in-phase (χ'_M, as $\chi'_M T$) and out-of-phase (χ''_M) ac magnetic susceptibility vs T for an undried microcrystalline sample of **3**·x(solv) at the indicated oscillation frequencies.
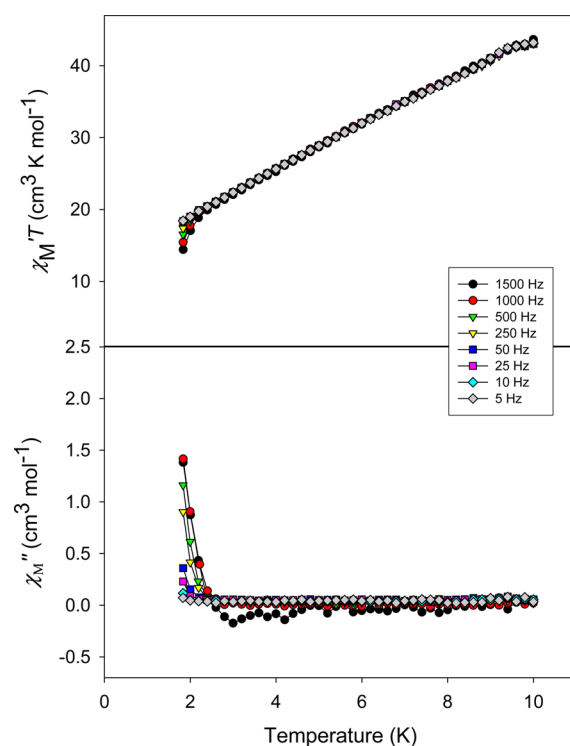
signals, the 1000 and 1500 Hz data showing peaks above 1.8 K, indicating the slow magnetization relaxation of a single-molecule magnet (SMM). Assuming that even for the 5 Hz

data the decrease in $\chi'_M T$ below ~2.5 K is all due to slow relaxation and/or weak intermolecular interactions the near-plateau data extrapolated to 0 K gives $\chi'_M T$ of 26–27 cm^3 K mol^{-1}, consistent with an $S = 7$ ground state; spin-only ($g = 2$) values for $S = 6$, 7, and 8 are 21, 28, and 36 cm^3 K mol^{-1}, respectively.

For **3**·x(solv), the $\chi'_M T$ vs T plot is noticeably different than for **2**·x(solv). It decreases more steeply, from 43.65 cm^3 K mol^{-1} at 10 K to a lower value of 20.68 cm^3 K mol^{-1} at 2.6 K, as excited states are depopulated. The 10 K value is higher than that for **2**·x(solv), again consistent with weaker coupling in **3** vs **2** and thus a greater population of excited states at 10 K. The decrease with decreasing T is near linear, and there is no sign of a plateauing of the data. Extrapolation to 0 K of the 5 Hz data gives a value of ~12−13 cm^3 K mol^{-1}, suggesting an $S = 5$ ground state with $g < 2$; spin-only values for $S = 4$ and 5 are 10 and 15 cm^3 K mol^{-1}, respectively. Below ~2.5 K, frequency-dependent decreases in $\chi'_M T$ are again observed, concomitant with the appearance of χ''_M signals indicating **3** to also be a SMM, but unlike **2**·x(solv) there are no peaks apparent above 1.8 K. The latter difference and the overall $\chi'_M T$ vs T profile are consistent with a smaller ground state and relaxation barrier for **3**·x(solv) vs **2**·x(solv). The possible SMM behavior of the two compounds suggested by the frequency-dependent $\chi'_M T$ and χ''_M signals were probed further by studies at lower T.

Magnetization Hysteresis Studies below 1.8 K. Magnetization vs dc field sweeps were performed with a micro-SQUID apparatus on single crystals of **2**·x(solv) and **3**·x(solv) freshly taken from mother liquor. The resulting data at different T and a 0.14 T/s sweep rate (Figure 9) show that both compounds exhibit hysteresis loops below 1.4 K, with coercivities (one-half the loop width at $M/M_S = 0$) increasing with decreasing T, as expected for the superparamagnet-like
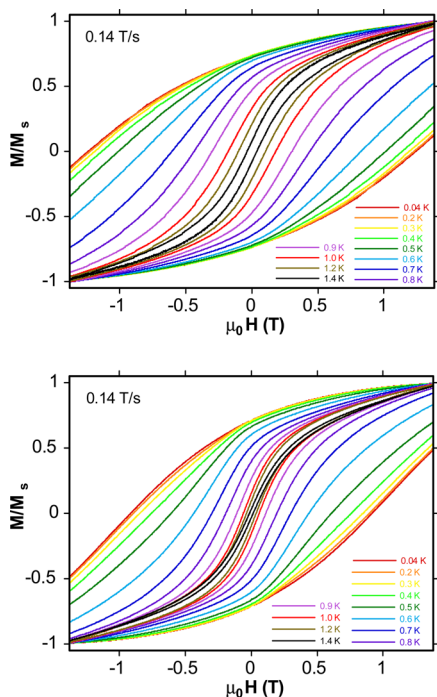
Figure 9. Magnetization (M) vs applied dc magnetic field ($\mu_0 H$) hysteresis loops at a 0.14 T/s sweep rate for single crystals (wet with mother liquor) of **2**·x(solv) (top) and **3**·x(solv) (bottom) at the indicated temperatures. M is normalized to its saturation value, M_s.

properties of a SMM. The coercivity for **2** is larger than that for **3** at each T, indicating the former to have the larger effective barrier (U_{eff}) to magnetization relaxation. The loops at 0.6 K at different sweep rates (Figure 10) show similar results, the
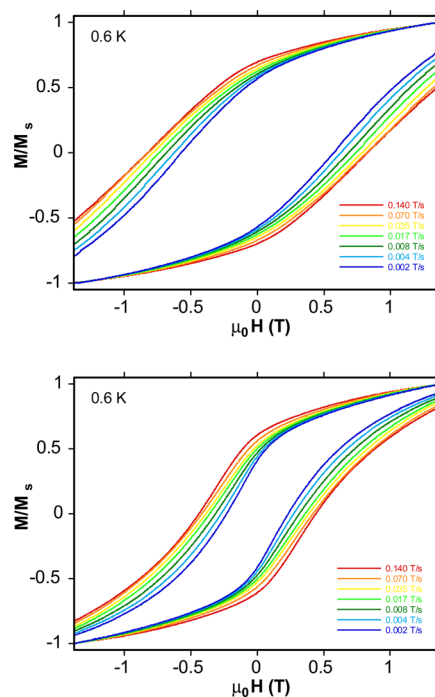
**Figure 10.** Magnetization (M) vs applied dc magnetic field ($\mu_0 H$) hysteresis loops at 0.6 K for single crystals (wet with mother liquor) of **2**·x(solv) (top) and **3**·x(solv) (bottom) at the indicated field sweep rates. M is normalized to its saturation value, M_s.

coercivity increasing with increasing sweep rate as expected for a SMM and the coercivity of **2** being greater than that for **3** at each sweep rate. Both compounds are thus confirmed as SMMs. The hysteresis loops do not display the step-like features indicative of QTM that are visible in the loops of smaller nuclearity SMMs, but this is due to the steps being smeared out by broadening effects arising primarily from the high density of low-lying excited states and also a distribution of relaxation barriers (i.e., a distribution of D values) consistent with a distribution of molecular environments from disordered ligands and the many solvent molecules. It is well recognized that even in much lower nuclearity SMMs, low-lying excited states and small environmental variations can smear out QTM steps. Thus, confirmation of the presence of QTM must be obtained by other means.[21,50] For example, below 0.2 K in Figure 9, the coercivity of the loops becomes temperature independent, suggesting the relaxation is now only by ground state tunneling between the lowest energy $m_s = \pm S$ levels of the spin S manifold.

To confirm this conclusion and to determine the relaxation barrier (U_{eff}), magnetization decay vs time studies were performed. The magnetization was first saturated in one direction by application of a large dc field at ~5 K, T was then lowered to a chosen value, the field was removed, and the magnetization decay was monitored with time (Figure S7). Analysis of the data yielded relaxation rate $1/\tau$ vs T data, where τ is the relaxation time, which were used to construct Arrhenius plots (Figure 11) based on eq 2

$$\tau = \tau_0 \exp(U_{eff}/kT) \qquad (2)$$
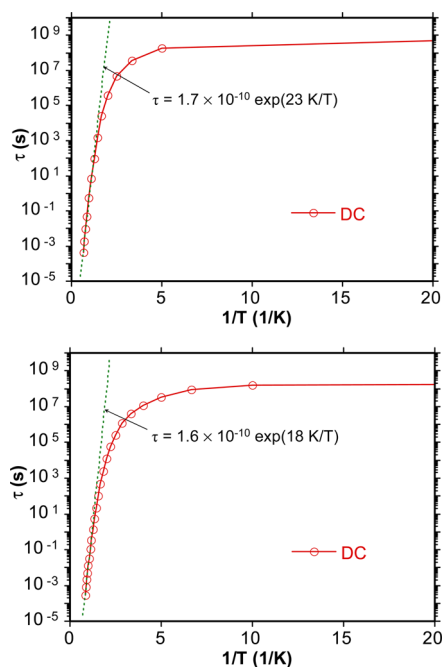
Figure 11. Arrhenius plot of the relaxation time (τ) vs $1/T$ for **2**·x(solv) (top) and **3**·x(solv) (bottom) using data obtained from single-crystal dc magnetization decay vs time measurements. The dashed line is the fit of the data in the thermally activated region to the Arrhenius relationship; see the text for the fit parameters.

where τ_0 is the inverse of the attempt frequency and k is the Boltzmann constant. The fit of the thermally activated region above ~0.5 K (dashed lines in Figure 11) gave U_{eff} = 23 K and $\tau_0 = 1.7 \times 10^{-10}$ s for **2**·x(solv) and U_{eff} = 18 K and $\tau_0 = 1.6 \times 10^{-10}$ for complex **3**·x(solv). For both complexes, the relaxation time begins leveling off below 0.5 K and below ~0.2 K becomes temperature independent, confirming relaxation only by QTM between the $m_s = \pm S$ levels of the ground state. Analogous QTM behavior was also observed for Mn$_{84}$.[21]

The bigger U_{eff} for **2** vs **3** by ~30% is consistent with the previous conclusion from dc and ac susceptibility data that the exchange coupling in **2** is slightly stronger on average than in **3** and that the ground state spin is slightly higher. We assume this is due to the different electronic properties of the alcohols employed and the small structural differences between **2** and **3** (particularly the two five-coordinate Mn^{III} in **2**) affecting the relative energies of the Mn magnetic orbitals and the resulting pairwise Mn$_2$ exchange couplings.

Mn$_{70}$ as a Classical Single-Domain Magnetic Nanoparticle. The above studies treated Mn$_{70}$ as a large, "bottom-up" molecule behaving as a quantum magnet, and the data were analyzed within that framework, revealing a small ground state S, a high density of excited states, and the occurrence of QTM. More detailed study of such large SMMs is extremely difficult given that the spin Hilbert space is vast, making it impossible, for example, to apply exact matrix diagonalization methods to such species. However, if SMMs are so large that they are comparable in size with the smaller "top-down" classical nanoparticles then it suggests that classical models frequently used to study the latter might be applicable, providing an alternative route to gaining a first-order level of understanding of such large molecular systems. We now describe application of the classical Néel–Brown model (NBM)[53] of thermally activated magnetization reversal of a single-domain magnetic particle to the Mn$_{70}$ SMMs, i.e., we will treat what is obviously a molecular system as a classical magnetic nanoparticle.

The NBM considers a single-domain magnetic nanoparticle undergoing thermally activated magnetization reversal between two equivalent ground states of opposite magnetization separated by an energy barrier arising from magnetic anisotropy. Its application to molecules is particularly attractive for high-nuclearity SMMs of large dimensions approaching the classical limit, i.e., having a high density of very low lying excited states and not exhibiting QTM steps in hysteresis loops. It would provide an alternative route for determining important magnetic parameters of the SMM, such as the energy barrier, the spin S, Arrhenius pre-exponential τ_0, and the cross-over temperature from the classical to the quantum regime. In contrast, EPR spectra of such large SMMs exhibit only very broad absorption peaks, allowing little characterization of the magnetic parameters.

In the classical NBM, the magnetic nanoparticle can relax from one ground state to the other by thermal activation over the barrier. At zero field and a sufficiently low T, the barrier is too large to allow this relaxation process, but it can be decreased by applying a field in the opposite direction to that of the particle's magnetization. When the applied field is similar to the reversal field, thermal fluctuations are sufficient to permit the particle to overcome the barrier and the magnetization reverses. This could in principle be studied by measuring the magnetization decay rate at many applied fields and temperatures to obtain the relaxation time τ, but this is very time consuming and fraught with many complications.[54] In addition, samples of traditional magnetic nanoparticles almost always involve a significant distribution of particle sizes, shapes, surface roughness, etc., and as a result yield a corresponding range of responses in magnetization decay vs T and H studies. One approach to get around this has been to study single nanoparticles, such as the ferromagnetic 20 nm Co metal nanoparticles that provided the first experimental demonstration of the NBM[54] and the ferrimagnetic 10−20 nm particles of BaFe$_{12−2x}$Co$_x$Ti$_x$O$_{19}$ that additionally provided evidence for macroscopic QTM.[55]

Crystals of Mn$_{70}$ provide a collection of magnetic nanoparticles of identical size, shape, and orientation and thus overcome the above distribution problems without recourse to single-molecule measurements. In addition, a more convenient method for studying the magnetization reversal is by ramping the applied field at a given rate and measuring the hysteresis coercive field H_c as a function of the field sweep rate and T.[54,56] A mathematical relationship between τ and reversal field probability was first given by Kurkijärvi[57] for the critical current in SQUIDs, and a more general calculation was provided by Garg.[58] Here, we approximate the mean reversal field of an ordered assembly of identical SMMs by the coercive field H_c (eq 3)

$$H_c = H_c^0(1 - [(k_B T/E_0)\ln(c/\nu)]^{1/2}) \qquad (3)$$

where ν is the field sweep rate dH/dt, H_c^0 is the coercive field at zero temperature, E_0 is the barrier height at zero applied field, and $c = H_c^0 k_B T/[2\tau_0 E_0(1 - H_c/H_c^0)]$.[54,56]

To apply the above method, the coercive fields H_c for a single crystal of **2**·x(solv) were measured at different T and ν and are plotted in Figure 12. As expected for a thermally activated
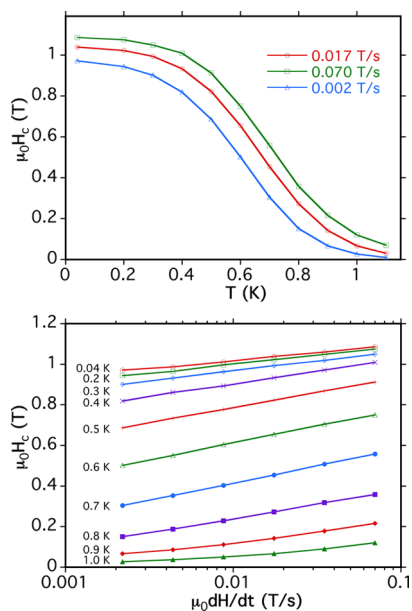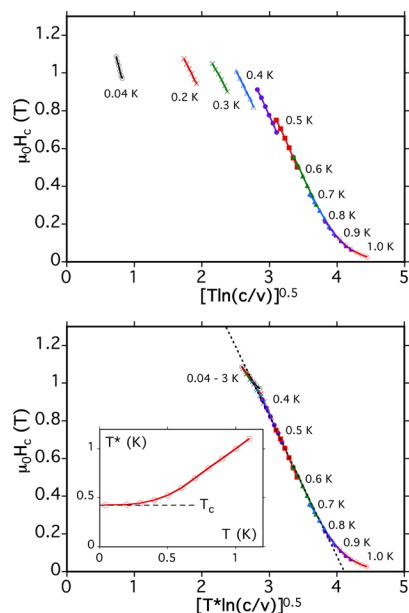
Figure 12. Coercive field H_c for a single crystal (wet with mother liquor) of **2**·x(solv) as a function of (top) temperature and (bottom) field sweep rate ν (= dH/dt).

Figure 13. (Top) Scaling plot of the coercive field H_c for a single crystal (wet with mother liquor) of **2**·x(solv) at field sweep rates ν between 0.001 and 0.1 T/s and at several temperatures. (Bottom) Same H_c data and same scales, but the real temperature T is replaced by an effective temperature T^* (see inset), which restores the scaling below 0.5 K.

process, H_c increases with decreasing T and increasing ν, and it becomes T independent below ~0.3 K. Furthermore, the data show an almost logarithmic dependence of H_c on the field sweep rate ν (Figure 12, bottom), consistent with eq 3. The validity of eq 3 was further tested by plotting the H_c values as a function of $[T \ln(c/\nu)]^{1/2}$. If the underlying model is adequate, all points should collapse onto one straight line by using the correct value for constant τ_0. Indeed, we found that almost all the H_c data fell on a master curve for $\tau_0 = 1.2 \times 10^{-7}$ s in Figure 13a, but large deviations are observed at the lowest T. In order to probe whether these are due to relaxation from the metastable potential well by tunneling, a common method used for classical systems is to replace the real temperature T by an effective temperature T^* in order to restore the scaling plot.[55] In the case of tunneling, T^* should saturate at low T. Indeed, the ansatz of T^*, as shown in the inset of Figure 13b, can restore unequivocally the scaling plot demonstrated by a straight master curve (Figure 13b). The flattening of T^* corresponds to a saturation of the relaxation rate, which is a necessary signature of tunneling. The cross-over temperature T_c can be defined as the T at which the quantum relaxation rate equals the thermal one; the inset of Figure 13b gives $T_c = 0.42$ K. The slopes and intercepts of the master curves give $E_0 = 17$ K and $H_c^0 = 3.1$ T, respectively. The E_0 is in reasonable agreement with the $U_{eff} = 23$ K obtained from the Arrhenius plot of Figure 11. The E_0 and H_c^0 values also allow the ground state spin of the "nanoparticle" to be estimated using eq 4.
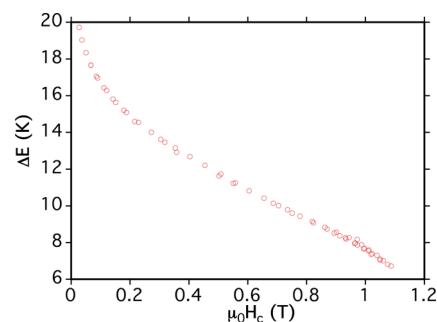
$$S = 2E_0/(g\mu_B\mu_0 H_c^0) \tag{4}$$

This gives a value of $S = 8$, which differs only slightly from the $S = 7$ estimated from ac susceptibility measurements, and the difference is attributed to quantum effects in the thermally activated regime that are not included in the model. Finally, the field dependence of the energy barrier (ΔE) can be obtained directly using eq 5 and is plotted in Figure 14.

$$\Delta E = k_B T \ln(c/\nu) \tag{5}$$

Figure 14. Field dependence of the energy barrier ΔE of **2**·x(solv) obtained using eq 4 and the set of $H_c(T,\nu)$ data in Figure 13.

Extrapolation to zero field provides an alternative estimation of the value of E_0 to be in the 20−25 K range, which is satisfyingly consistent with the $U_{eff} = 23$ K from Figure 11.

Comparison with Other Giant Wheel Molecules. The Mn$_{70}$ clusters **2** and **3** were compared with Mn$_{84}$ earlier, and they also join a very small group of giant wheel molecules with a torus structure for other metals. In fact, the first ones to be discovered were in Mo chemistry,[59] with the largest currently known being the Mo$_{154}$[60] and Mo$_{176}$[61] compounds prepared by Müller and co-workers. Although they have significantly higher nuclearities, their diameters of ~3.4 and ~4.1 nm, respectively, are comparable to the ~3.7/~4.1 nm of **2/3** and ~4.3 nm of Mn$_{84}$. These and other giant polyoxometallates[62] are diamagnetic or nearly so, and none of them exhibit SMM properties. The same is true for the recently reported Pd$_{84}$ wheel with a torus structure.[63] It is remarkably similar to the Mn$_{84}$ in nuclearity and has a diameter of ~3 nm and thickness ~1 nm. However, unlike Mn$_{70}$ and Mn$_{84}$, which have five and six Mn$_{14}$ repeating units and thus D_{5d} and D_{6d} symmetry, respectively, it has seven Pd$_{12}$ repeating units and overall D_{7d} symmetry. The same is found for Mo$_{154}$, which has seven Mo$_{22}$

repeating units. On the basis of changes to the number of repeating units, the authors predicted that Pd_{60}, Pd_{72}, and Pd_{96} clusters might be capable of synthesis with similar wheel or other structures. For the Mn case, we have now shown that two members of the $[Mn_{14}]_n$ family of related wheels with $n = 5$ and 6 can be obtained from reactions under mild conditions and by simple variation in the identity of the ligation environment and have commented that the Mn_{56} and Mn_{98} members might also be accessible.

CONCLUSIONS

The molecular approach to nanoscale magnets has led to the discovery of Mn_{70} clusters with a torus structure of ~3.7–4.1 nm diameter, expanding this family of $[Mn_{14}]_n$ wheels to two nuclearities. These new Mn_{70} giant clusters have also been shown to be SMMs displaying magnetization hysteresis, the diagnostic classical property of a magnet, as well as QTM, the property of the quantum world. Thus, in both their size and their magnetic properties, the Mn_{70} clusters can be accurately described as being mesoscale particles at the interface of the bottom-up and top-down worlds of nanomagnetism, bringing the molecular advantage of highly ordered crystalline arrays of monodisperse species to this interface. In support of this mesoscale description of Mn_{70}, the classical Néel–Brown model has been employed as an alternative route to determining characteristic parameters of the magnetization relaxation dynamics of such large SMMs, involving the study of the temperature and field sweep rate dependences of the coercive field. The successful application of this classical model emphasizes the approach of Mn_{70} to the classical–quantum interface. This is thus a very useful tool for magnetically characterizing molecular systems of such large size and complexity that they do not permit a detailed understanding at the quantum level. We also consider that the field of giant Mn/O SMMs may be much larger than originally thought and that additional members with torus or other structures are likely to be amenable to synthesis. Attempts to attain them are therefore under investigation.

ASSOCIATED CONTENT

⑤ Supporting Information

The Supporting Information is available free of charge on the ACS Publications website at DOI: 10.1021/acs.inorgchem.5b02790.

Bond valence sums, bond distances and angles, magnetic data (PDF)

Crystallographic details in CIF format (CIF)

AUTHOR INFORMATION

Corresponding Author

*E-mail: christou@chem.ufl.edu.

Present Address

§Department of Chemistry, University of Cyprus, P.O. Box 20537, 1678 Nicosia, Cyprus.

Notes

The authors declare no competing financial interest.

ACKNOWLEDGMENTS

REFERENCES

(1) (a) Christou, G.; Gatteschi, D.; Hendrickson, D. N.; Sessoli, R. *MRS Bull.* **2000**, *25*, 66−71. (b) Gatteschi, D.; Sessoli, R. *Angew. Chem., Int. Ed.* **2003**, *42*, 268−297. (c) Sessoli, R.; Tsai, H. − L.; Schake, A. R.; Wang, S.; Vincent, J. B.; Folting, K.; Gatteschi, D.; Christou, G.; Hendrickson, D. N. *J. Am. Chem. Soc.* **1993**, *115*, 1804. (d) Sessoli, R.; Gatteschi, D.; Caneschi, A.; Novak, M. A. *Nature* **1993**, *365*, 141.

(2) (a) Woodruff, D. N.; Winpenny, R. E.; Layfield, R. A. *Chem. Rev.* **2013**, *113*, 5110−5148. (b) Aromi, G.; Brechin, E. K. *Struct. Bonding (Berlin)* **2006**, *122*, 1−67.

(3) (a) Christou, G. *Polyhedron* **2005**, *24*, 2065−2075. (b) Bagai, R.; Christou, G. *Chem. Soc. Rev.* **2009**, *38*, 1011−1026.

(4) (a) Rinehart, J. D.; Fang, M.; Evans, W. J.; Long, J. R. *Nat. Chem.* **2011**, *3*, 538−542. (b) Rinehart, J. D.; Fang, M.; Evans, W. J.; Long, J. R. *J. Am. Chem. Soc.* **2011**, *133*, 14236−14239.

(5) Friedman, J. R.; Sarachik, M. P.; Tejada, J.; Ziolo, R. *Phys. Rev. Lett.* **1996**, *76*, 3830−3833.

(6) Thomas, L.; Lionti, F.; Ballou, R.; Gatteschi, D.; Sessoli, R.; Barbara, B. *Nature* **1996**, *383*, 145−147.

(7) Wernsdorfer, W.; Bhaduri, S.; Tiron, R.; Hendrickson, D. N.; Christou, G. *Phys. Rev. Lett.* **2002**, *89*, 197201.

(8) Wernsdorfer, W.; Aliaga-Alcalde, N.; Hendrickson, D. N.; Christou, G. *Nature* **2002**, *416*, 406−409.

(9) (a) Hill, S.; Edwards, R. S.; Aliaga-Alcalde, N.; Christou, G. *Science* **2003**, *302*, 1015−1018. (b) Tiron, R.; Wernsdorfer, W.; Foguet-Albiol, D.; Aliaga-Alcalde, N.; Christou, G. *Phys. Rev. Lett.* **2003**, *91*, 227203.

(10) (a) Wernsdorfer, W.; Sessoli, R. *Science* **1999**, *284*, 133−135. (b) Wernsdorfer, W.; Chakov, N. E.; Christou, G. *Phys. Rev. Lett.* **2005**, *95*, 037203.

(11) Leuenberger, M. N.; Loss, D. *Nature* **2001**, *410*, 789.

(12) Zhou, B.; Tao, R.; Shen, S.-Q.; Liang, J.-Q. *Phys. Rev. A: At., Mol., Opt. Phys.* **2002**, *66*, 010301.

(13) Affronte, M.; Troiani, F.; Ghirri, A.; Candini, A.; Evangelisti, M.; Corradini, V.; Carretta, S.; Santini, P.; Amoretti, G.; Tuna, F.; Timco, G.; Winpenny, R. E. P. *J. Phys. D: Appl. Phys.* **2007**, *40*, 2999.

(14) Vincent, R.; Klyatskaya, S.; Ruben, M.; Wernsdorfer, W.; Balestro, F. *Nature* **2012**, *488*, 357.

(15) Bogani, L.; Wernsdorfer, W. *Nat. Mater.* **2008**, *7*, 179.

(16) (a) Katoh, K.; Isshiki, H.; Komeda, T.; Yamashita, M. *Chem. - Asian J.* **2012**, *7*, 1154. (b) Katoh, K.; Isshiki, H.; Komeda, T.; Yamashita, M. *Coord. Chem. Rev.* **2011**, *255*, 2124.

(17) (a) Barbara, B.; Chudnovsky, E. M. *Phys. Lett. A* **1990**, *145*, 205−208. (b) Gider, S.; Awschalom, D. D.; Douglas, T.; Mann, S.; Chaparala, M. *Science* **1995**, *268*, 77−80.

(18) (a) Batlle, X.; Labarta, A. *J. Phys. D: Appl. Phys.* **2002**, *35*, R15. (b) Sorensen, C. M. *Magnetism in Nanoscale Materials in Chemistry*; Klabunde, K. J., Eds.; Wiley-Interscience: New York, 2001.

(19) (a) Lu, A.-H.; Salabas, E. L.; Schüth, F. *Angew. Chem., Int. Ed.* **2007**, *46*, 1222−1244. (b) Hyeon, T. *Chem. Commun.* **2003**, 927−934. (c) Laurent, S.; Forge, D.; Port, M.; Roch, A.; Robic, C.; Vander Elst, L.; Muller, R. N. *Chem. Rev.* **2008**, *108*, 2064−2110.

(20) Jamet, M.; Wernsdorfer, W.; Thirion, C.; Mailly, D.; Dupuis, V.; Mélinon, P.; Pérez, A. *Phys. Rev. Lett.* **2001**, *86*, 4676.

(21) Tasiopoulos, A. J.; Vinslava, A.; Wernsdorfer, W.; Abboud, K. A.; Christou, G. *Angew. Chem., Int. Ed.* **2004**, *43*, 2117.

(22) Liu, T.; Zhang, Y.-J.; Wang, Z.-M.; Gao, S. *J. Am. Chem. Soc.* **2008**, *130*, 10500−10501.

(23) Peng, J.-B.; Kong, X.-J.; Zhang, Q.-C.; Orendáč, M.; Prokleška, J.; Ren, Y.-P.; Long, L.-S.; Zheng, Z.; Zheng, L.-S. *J. Am. Chem. Soc.* **2014**, *136*, 17938−17941.

(24) Kong, X.-J.; Long, L.-S.; Huang, R.-B.; Zheng, L.-S.; Harris, T. D.; Zheng, Z. *Chem. Commun.* **2009**, 4354−4356.

(25) Kong, X.-J.; Ren, Y.-P.; Chen, W.-X.; Long, L.-S.; Zheng, Z.; Huang, R.-B.; Zheng, L.-S. *Angew. Chem., Int. Ed.* **2008**, *47*, 2398−2401.

(26) Leng, J.-D.; Liu, J.-L.; Tong, M.-L. *Chem. Commun.* **2012**, *48*, 5286−5288.

(27) Wernsdorfer, W. *Adv. Chem. Phys.* **2001**, *118*, 99−190.

(28) Lis, T. *Acta Crystallogr., Sect. B: Struct. Crystallogr. Cryst. Chem.* **1980**, *36*, 2042.

(29) (a) Sala, T.; Sargent, M. V. *J. Chem. Soc., Chem. Commun.* **1978**, 253. (b) Vincent, J. B.; Chang, H. R.; Folting, K.; Huffman, J. C.; Christou, G.; Hendrickson, D. N. *J. Am. Chem. Soc.* **1987**, *109*, 5703.

(30) Sheldrick, G. M. *SHELXTL6*; Bruker Analytical X-ray Systems: Madison, WI, 2000.

(31) Spek, A. L. *Acta Crystallogr., Sect. D: Biol. Crystallogr.* **2009**, *65*, 148−155.

(32) Wernsdorfer, W. *Adv. Chem. Phys.* **2001**, *118*, 99.

(33) (a) Jones, L. F.; Brechin, E. K.; Collison, D.; Raftery, J.; Teat, S. J. *Inorg. Chem.* **2003**, *42*, 6971. (b) Jones, L. F.; Rajaraman, G.; Brockman, J.; Murugesu, M.; Raftery, J.; Teat, S. J.; Wernsdorfer, W.; Christou, G.; Brechin, E. K.; Collison, D. *Chem. - Eur. J.* **2004**, *10*, 5180. (c) Dendrinou-Samara, C.; Zaleski, C. M.; Evagorou, A.; Kampf, J. W.; Pecoraro, V. L.; Kessissoglou, D. P. *Chem. Commun.* **2003**, 2668. (d) Brechin, E. K.; Clegg, W.; Murrie, M.; Parsons, S.; Teat, S. J.; Winpenny, R. E. P. *J. Am. Chem. Soc.* **1998**, *120*, 7365.

(34) (a) Pohl, I. A. M.; Westin, L. G.; Kritikos, M. *Chem. - Eur. J.* **2001**, *7*, 3438. (b) Murugesu, M.; Habrych, M.; Wernsdorfer, W.; Abboud, K. A.; Christou, G. *J. Am. Chem. Soc.* **2004**, *126*, 4766. (c) Jones, L. F.; Brechin, E. K.; Collison, D.; Harrison, A.; Teat, S. J.; Wernsdorfer, W. *Chem. Commun.* **2002**, 2974.

(35) (a) Milios, C. J.; Raptopoulou, C. P.; Terzis, A.; Lloret, F.; Vicente, R.; Perlepes, S. P.; Escuer, A. *Angew. Chem., Int. Ed.* **2004**, *43*, 210. (b) Mukhopadhyay, S.; Gandhi, B. A.; Kirk, M. L.; Armstrong, W. H. *Inorg. Chem.* **2003**, *42*, 8171. (c) Price, D. J.; Batten, S. R.; Moubaraki, B.; Murray, K. S. *Chem. Commun.* **2002**, 762.

(36) (a) Brockman, J. T.; Huffman, J. C.; Christou, G. *Angew. Chem., Int. Ed.* **2002**, *41*, 2506. (b) Murugesu, M.; Raftery, J.; Wernsdorfer, W.; Christou, G.; Brechin, E. K. *Inorg. Chem.* **2004**, *43*, 4203.

(37) (a) Tasiopoulos, A. J.; Wernsdorfer, W.; Abboud, K. A.; Christou, G. *Angew. Chem., Int. Ed.* **2004**, *43*, 6338. (b) King, P.; Wernsdorfer, W.; Abboud, K. A.; Christou, G. *Inorg. Chem.* **2004**, *43*, 7315.

(38) (a) Tasiopoulos, A. J.; Wernsdorfer, W.; Abboud, K. A.; Christou, G. *Inorg. Chem.* **2005**, *44*, 6324. (b) King, P.; Wernsdorfer, W.; Abboud, K. A.; Christou, G. *Inorg. Chem.* **2005**, *44*, 8659−8669.

(39) See Supporting Information.

(40) Liu, W.; Thorp, H. H. *Inorg. Chem.* **1993**, *32*, 4102.

(41) Mn BVS values for **2** were all in the 2.8−3.1 range.

(42) (a) Brown, I. D.; Shannon, R. D. *Acta Crystallogr., Sect. A: Cryst. Phys., Diffr., Theor. Gen. Crystallogr.* **1973**, *29*, 266. (b) Donnay, G.; Allman, R. *Am. Mineral.* **1970**, *55*, 1003.

(43) O BVS values for **2** were in the 1.73−1.95 for $O^{2−}$, 0.21−0.28 for H_2O, 1.58−1.84 for EtO⁻, and 0.92−1.34 for EtOH.

(44) Mn BVS values for **3** were all in the 2.8−3.0 range.

(45) O BVS values for **3** were in the 1.63−1.97 for $O^{2−}$, 0.20−0.28 for H_2O, 1.75−1.89 for $ClC_2H_4O^−$, and 1.00−1.68 for ClC_2H_4OH.

(46) Moushi, E. E.; Lampropoulos, C.; Wernsdorfer, W.; Nastopoulos, V.; Christou, G.; Tasiopoulos, A. J. *J. Am. Chem. Soc.* **2010**, *132*, 16146−16155.

(47) Scott, R. T. W.; Parsons, S.; Murugesu, M.; Wernsdorfer, W.; Christou, G.; Brechin, E. K. *Angew. Chem., Int. Ed.* **2005**, *44*, 6540−6543.

(48) Manoli, M.; Inglis, R.; Manos, M. J.; Nastopoulos, V.; Wernsdorfer, W.; Brechin, E. K.; Tasiopoulos, A. J. *Angew. Chem., Int. Ed.* **2011**, *50*, 4441 (b).

(49) Langley, S. K.; Stott, R. A.; Chilton, N. F.; Moubaraki, B.; Murray, K. S. *Chem. Commun.* **2011**, *47*, 6281.

(50) Soler, M.; Wernsdorfer, W.; Folting, K.; Pink, M.; Christou, G. *J. Am. Chem. Soc.* **2004**, *126*, 2156.

(51) Perlepes, S. P.; Huffman, J. C.; Christou, G. *J. Chem. Soc., Chem. Commun.* **1991**, *23*, 1657−1659.

(52) Davidson, E. R. *MAGNET*; Indiana University: Bloomington, IN, 1999.

(53) (a) Néel, L. *Ann. Geophys.* **1949**, *5*, 99. (b) Brown, W. F. *Phys. Rev.* **1963**, *130*, 1677.

(54) Wernsdorfer, W.; Bonet Orozco, E.; Hasselbach, K.; Benoit, A.; Barbara, B.; Demoncy, N.; Loiseau, A.; Boivin, D.; Pascard, H.; Mailly, D. *Phys. Rev. Lett.* **1997**, *78*, 1791.

(55) Wernsdorfer, W.; Bonet Orozco, E.; Hasselbach, K.; Benoit, A.; Mailly, D.; Kubo, O.; Nakano, H.; Barbara, B. *Phys. Rev. Lett.* **1997**, *79*, 4014.

(56) Wernsdorfer, W.; Murugesu, M.; Tasiopoulos, A. J.; Christou, G. *Phys. Rev. B: Condens. Matter Mater. Phys.* **2005**, *72*, 212406.

(57) Kurkijärvi, J. *Phys. Rev. B* **1972**, *6*, 832.

(58) Garg, A. *Phys. Rev. B: Condens. Matter Mater. Phys.* **1995**, *51*, 15592.

(59) Dolbecq, A.; Sécheresse, F. *Adv. Inorg. Chem.* **2002**, *53*, 1.

(60) Müller, A.; Krickemeyer, E.; Meyer, J.; Bögge, H.; Peters, F.; Plass, W.; Diemann, E.; Dillinger, S.; Nonnenbruch, F.; Randerath, M.; Menke, C. *Angew. Chem., Int. Ed. Engl.* **1995**, *34*, 2122.

(61) Müller, A.; Krickemeyer, E.; Bögge, H.; Schmidtmann, M.; Beugholt, C.; Kögerler, P.; Lu, C. *Angew. Chem., Int. Ed.* **1998**, *37*, 1220.

(62) (a) Müller, A.; Shah, S. Q. N.; Bögge, H.; Schmidtmann, M. *Nature* **1999**, *397*, 48. (b) Müller, A.; Roy, S. *Russ. Chem. Rev.* **2002**, *71*, 981. (c) Müller, A.; Kögerler, P.; Dress, A. W. M. *Coord. Chem. Rev.* **2001**, *222*, 193.

(63) (a) Xu, F.; Miras, H. N.; Scullion, R. A.; Long, D.-L.; Thiel, J.; Cronin, L. *Proc. Natl. Acad. Sci. U. S. A.* **2012**, *109*, 11609−11612. (b) Scullion, R. A.; Surman, A. J.; Xu, F.; Mathieson, J. S.; Long, D.-L.; Haso, F.; Liu, T.; Cronin, L. *Angew. Chem., Int. Ed.* **2014**, *53*, 10032−10037.